



















Twilight Mesospheric Clouds in Jezero as Observed by MEDA Radiation and Dust Sensor (RDS)



Key Points:

- Most of the cloud detected at twilight between sol 71 and 492 of the Mars 2020 mission (Ls 39°–262°) occurred at altitudes between 40 and 50 km
- Around aphelion (Ls ~ 70°) we found the minimum in cloud activity and lower cloud opacities
- The cloud activity at sunrise is slightly stronger than at sunset and this is likely due to the lower temperatures

D. Toledo¹ , L. Gómez¹ , V. Apéstigue¹ , I. Arruego¹ , M. Smith² ,
A. Manguira³ , G. Martínez⁴ , P. Patel⁵ , A. Sanchez-Lavega³ , M. Lemmon⁶ , L. Tamppari⁵ ,
D. Viudez-Moreiras⁷ , R. Hueso³ , A. Vicente-Retortillo⁷ , C. Newman⁸ , R. Lorenz⁹ ,
M. Yela¹ , M. de la Torre Juarez⁵ , and J. A. Rodriguez-Manfredi⁷

¹Instituto Nacional de Técnica Aeroespacial (INTA), Madrid, Spain, ²NASA Godard Space Flight Center, Greenbelt, MD, USA, ³Universidad del País Vasco UPV/EHU, Bilbao, Spain, ⁴Lunar and Planetary Institute, Universities Space Research Association, Houston, TX, USA, ⁵Jet Propulsion Laboratory, California Institute of Technology, Pasadena, CA, USA, ⁶Space Science Institute, Boulder, CO, USA, ⁷Centro de Astrobiología (INTA-CSIC), Torrejón de Ardoz, Madrid, Spain, ⁸Aeolis Research, Chandler, AZ, USA, ⁹Johns Hopkins Applied Physics Laboratory, Laurel, MD, USA

Correspondence to:

D. Toledo,
toledoc@inta.es

Citation:

Toledo, D., Gómez, L., Apéstigue, V., Arruego, I., Smith, M., Manguira, A., et al. (2023). Twilight mesospheric clouds in Jezero as observed by MEDA Radiation and Dust Sensor (RDS). *Journal of Geophysical Research: Planets*, 128, e2023JE007785. <https://doi.org/10.1029/2023JE007785>

Received 11 FEB 2023
Accepted 22 JUN 2023

Abstract The Mars Environmental Dynamics Analyzer instrument, on board NASA's Mars 2020 Perseverance rover, includes a number of sensors to characterize the Martian atmosphere. One of these sensors is the Radiation and Dust Sensor (RDS) that measures the solar irradiance at different wavelengths and geometries. We analyzed the RDS observations made during twilight for the period between sol 71 and 492 of the mission (Ls 39°–262°, Mars Year 36) to characterize the clouds over the Perseverance rover site. Using the ratio between the irradiance at zenith at 450 and 750 nm, we inferred that the main constituent of the detected high-altitude aerosol layers was ice from Ls = 39°–150° (cloudy period), and dust from Ls 150°–262°. A total of 161 twilights were analyzed in the cloudy period using a radiative transfer code and we found: (a) signatures of clouds/hazes in the signals in 58% of the twilights; (b) most of the clouds had altitudes between 40 and 50 km, suggesting water ice composition, and had particle sizes between 0.6 and 2 μm; (c) the cloud activity at sunrise is slightly higher than at sunset, likely due to the differences in temperature; (d) the time period with more cloud detections and with the greatest cloud opacities is during Ls 120°–150°; and (e) a notable decrease in the cloud activity around aphelion, along with lower cloud altitudes and opacities. This decrease in cloud activity indicates lower concentrations of water vapor or cloud condensation nuclei (dust) around this period in the Martian mesosphere.

Plain Language Summary During twilight, ground-based observations of the irradiance allows the detection and characterization of high-altitude clouds (above 30–35 km). Because the sun is at or below the horizon, the cloud layers reflect the direct light that only reaches the higher parts of the atmosphere, producing an increase in the sky brightness with respect to the cloud-free scenario. Moreover, the decrease in the intensity with the solar zenith angle highly depends on the cloud altitude and density. Using observations made by the Radiation and Dust Sensor, part of the instrument Mars Environmental Dynamics Analyzer on board Perseverance rover, we present here a study of the twilight clouds detected at the Perseverance landing site for the first 490 sols of the mission (Mars Year 36). By modeling the irradiance at 450 and 950 nm with radiative transfer simulations, we constrained the cloud altitude, opacity, and particle radius. The number of twilights analyzed allowed us to study the seasonal trend in the cloud activity. During the cloudy period, Ls 39°–150°, we find a significant decrease in the cloud activity above 30–35 km around aphelion (Ls ~ 70°). This implies that the seasonal distribution of clouds above 30–35 km differs from that observed at lower altitudes.

1. Introduction

The H₂O and CO₂ ice clouds on Mars are primary constituents studied for understanding the past and present climate of the planet (Forget & Pierrehumbert, 1997; Montmessin et al., 2004). Cloud particles can affect the energy balance of the planet (e.g., Wolff et al., 2019), and thus the atmospheric dynamics, as well as influence the vertical distribution of dust particles through dust scavenging. The dust scavenging by H₂O clouds has critical consequences in the water cycle of the planet; for example, regions in the atmosphere with insufficient quantity of dust particles (or condensation nuclei) can inhibit the formation of H₂O clouds (Määttä et al., 2005; Montmessin et al., 2002), and thus reach water vapor concentrations in excess of saturation (Maltagliati et al., 2011; Navarro

© 2023 The Authors.

This is an open access article under the terms of the [Creative Commons Attribution-NonCommercial License](https://creativecommons.org/licenses/by-nc/4.0/), which permits use, distribution and reproduction in any medium, provided the original work is properly cited and is not used for commercial purposes.

et al., 2014). Although other mechanisms may be responsible for the existence of supersaturation on Mars as well (Fedorova et al., 2020), it is well established that the formation of clouds limits the concentration of water vapor to values below saturation, and this partially controls the amount of water vapor that can be transported to the higher parts of the atmosphere, where the water can be photodissociated into its lighter components H and O.

One of the two major cloud regimes on Mars is the aphelion cloud belt (ACB) (Clancy et al., 1996) occurring in the equatorial regions between $\sim 10^{\circ}\text{S}$ and $\sim 30^{\circ}\text{N}$ and during the northern spring and summer ($L_s \sim 0^{\circ}$ – 180°). The other main cloud regime is the hoods over the polar cap in both hemispheres (Benson et al., 2010, 2011) during late summer and the whole winter (these clouds are not studied in this work). As reported in many previous works, both events are observed every Martian year (MY). Although H_2O and CO_2 clouds or hazes have been observed and studied from the surface of Mars, directly through images or indirectly through aerosol opacity measurements (e.g., Lemmon et al., 2015; Lorenz et al., 2020; P. H. Smith & Lemmon, 1999), the longest record of cloud events comes from instrumentation onboard orbiters (e.g., Määttä et al., 2010; McConnochie et al., 2010; Sánchez-Lavega et al., 2018; Tamppari et al., 2003; Wang & Ingersoll, 2002; Wolff et al., 2022). When these orbiter observations are made at limb-viewing geometry, information on the cloud vertical profiles can be derived (e.g., Rannou et al., 2006; M. D. Smith et al., 2013). In these particular cases the cloud frequency-of-occurrence or properties (e.g., opacity, particle radius) can be studied as a function of the altitude. On the other hand, if the orbiter observations are obtained at nadir-viewing geometry, in general the cloud vertical profiles cannot be derived and the total ice column opacity is provided (e.g., Giuranna et al., 2021; M. D. Smith, 2009). While orbital observations provide a more complete global coverage, landed observations represent a critically important component to: (a) cross validate the orbital observations and retrievals; (b) study the diurnal and seasonal variations of the cloud activity without the impact of the orbiter spatial and temporal sampling; and (c) investigate the atmospheric context in which the clouds were formed (if observations of meteorological time series are available).

On 18 February 2021, the Mars 2020 rover Perseverance successfully landed in Jezero crater (latitude 18.44°N and longitude 77.45°E). To provide meteorological context for other observations and for future human exploration, Perseverance carries the Mars Environmental Dynamics Analyzer (MEDA) (Rodríguez-Manfredi et al., 2021) instrument, which includes a set of sensors: two wind sensors to infer wind direction and speed, five thermal sensors at different locations and heights (ATS), an infrared radiometer to measure ground and atmospheric temperature as well as atmospheric IR fluxes and reflected solar fluxes (TIRS), a relative humidity sensor, a pressure sensor, and the Radiation and Dust Sensor (RDS) that measures the solar radiation at different wavelengths ranges from the UVA to the near infrared (Rodríguez-Manfredi et al., 2021, 2023). In this paper we focus on RDS observations at twilight, when the solar zenith angle (SZA) is between 90° and 98° , to detect and characterize high-altitude clouds (above ~ 30 km) for the first 492 sols of the mission (MY 36). We briefly describe the RDS in Section 2, as well as the observations, the principle of measurement and the radiative transfer (RT) modeling. In Section 3, we present time series of high-altitude aerosol layers (ALs) detected during twilight, the cloud retrievals and main results.

2. Observations and Radiative Transfer Modeling

2.1. RDS Instrument

RDS measures the solar irradiance at different spectral wavelengths and incident geometries. It is comprised of two sets of photodetectors (RDS-DP) and a camera pointing at zenith (RDS-SkyCam). The first set of photodetectors, the Top channels, corresponds to eight zenith-pointed detectors which cover the light spectrum from UVA to Near IR (Top-1 to Top-8: 255, 259, 250–400, 450, 650, 750, 190–1,100, and 950 nm). Most of the Top detectors use interferential filters and mechanical masks (Apestigue et al., 2022) to constrain their field of view to $\pm 15^{\circ}$ zenith angle, while the Top-7 channel covers the full sky from 0° to 90° zenith angle and for all azimuth angles. The second set corresponds to the eight Lateral channels, which are pointed sideways at 20° (except Lat-8, which is 35°) above the rover deck and are all at 750 nm. The Lat-1 channel is blinded to study the photodetector performance degradation. In this work only the observations made by the Top sensors will be used. In general, MEDA sampling is set at 1 Hz with all sensors operating for blocks of 1 hr and 5 min. The disposition of the blocks along the day are selected for each sol based on a cadence that alternates even and odd hours, and the duration and number of block sometimes change depending on power availability and data volume constraints. For this reason, not all the twilights are covered by MEDA. Because of the low levels of irradiance expected during this

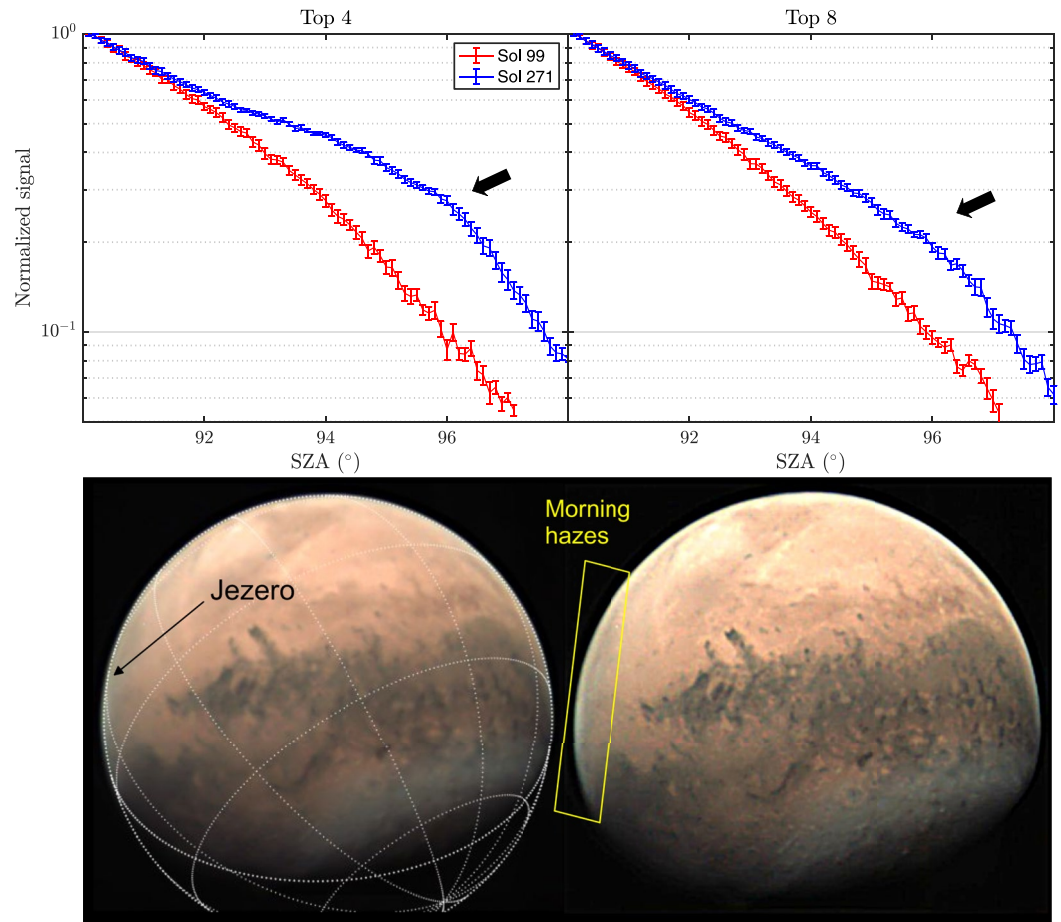


Figure 1. The upper panels show a comparison between Radiation and Dust Sensor (RDS) observations at 450 (Top 4) and 950 nm (Top 8) made under cloud-free conditions (sol 99) and under the presence of clouds (sol 271). The presence of the clouds result in an increase in the irradiance (indicated with the black arrows). Note that each signal was normalized by the signal value at solar zenith angle = 90°. By doing so, we diminish the impact of the dust opacity and particle radius on the RDS signals, and make the comparison between signals easier to interpret. As we will see in the following section, the normalization of the signals also allow us to reduce the number of free parameters in the radiative transfer analysis. The presence of clouds (or hazes) on sol 271 at sunrise was also confirmed by images taken by the Visual Monitoring Camera (VMC) (Sánchez-Lavega et al., 2018) onboard Mars Express (lower panel). In the VMC images we see that Jezero crater (indicated with the black arrow) was overcast by bright morning limb clouds or hazes.

time of the day, these RDS observations are acquired with an extra 40 gain factor (Apestigue et al., 2022), which is activated when $SZA \geq 90^\circ$. Note that because the RDS gain factor was not activated until sol 70, our analysis does not cover the first sols of the mission.

2.2. Principle of Measurement for the Detection of Clouds

Since high-altitude ALs (e.g., H₂O clouds or detached dust layers) imply an increase in the irradiance during twilight, clouds can be detected by looking at the evolution of the RDS Top observations at SZAs between 90° and 98° (~30 min long). Moreover, during this period only the higher parts of the atmosphere receive Sun direct light (as for altitudes $< R(1 + \tan^2(90^\circ - SZA))^{0.5}$, where R is the radius of the planet, the direct light intersects the planet surface), making the variation of the irradiance with SZA very sensitive to cloud properties such as the altitude or the number density. As indicated in Toledo, Rannou, Pommereau, Sarkissian, and Foujols (2016), this technique allows detecting clouds with very low opacities (subvisual opacities), as the pathway of sunlight in a horizontally homogeneous AL of h geometrical thickness is enhanced by a factor $> 1/\sin(SZA - 90^\circ)$. Figure 1 shows, as an example, RDS signals measured by Top-4 (450 ± 10 nm) and Top-8 (950 ± 10 nm) sensors at

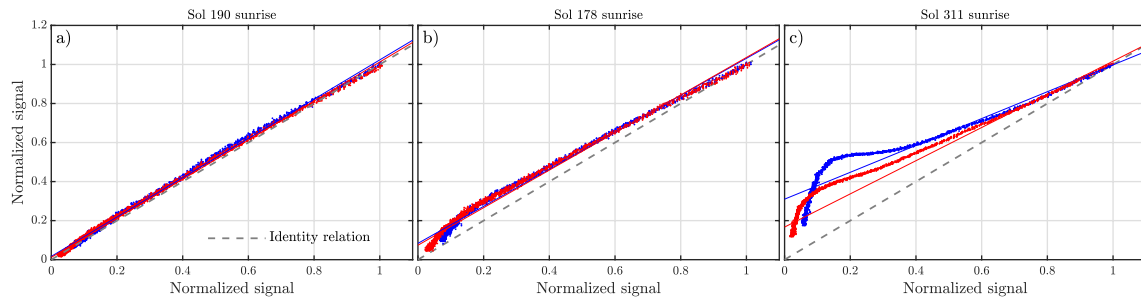


Figure 2. Correlation between the Radiation and Dust Sensor signals at 450 (blue) and 950 nm (red) measured for a cloud-free day, represented in the x -axis, and during the dawn of (a) sol 190, (b) 178, and (c) 311, represented in the y -axis. For each twilight we derived two correlation plots, one per channel, whose measurements are compared with the signals measured under cloud-free conditions for the same solar zenith angles. The correlation curves were fitted to a straight line (solid lines in blue and red for the Top 4 and Top 8 channels, respectively) whose slope is used to infer the presence of aerosol layer. The gray dashed line represents the identity relation.

twilight for a cloud free day and for a day with the presence of clouds (also confirmed by orbiter observations). We observe that the clouds produce an increase in the irradiance (indicated by the black arrows) with respect to the scenario without clouds, and thus by comparing each twilight recorded by the RDS with the signals for the cloud-free scenario, we can infer on what sols of the mission there were clouds (or high dust layers) present during this period of the day.

An easy way to determine when cloud features are present in the RDS observations is to compare the Top-4 and Top-8 signals for each twilight with those for the cloud-free day of Figure 1 (red lines and referred hereafter as the reference signals). Figure 2 shows, as an example, the correlation between the twilight RDS signals at 450 and 950 nm and the reference signals (at the same wavelengths and SZAs) for three different sunrises. The two correlation curves (one for Top-4 and another for Top-8) derived for each sunrise were fitted to a straight line, whose slopes were compared with the identity relation (gray dashed line). If the slopes are close to 1, then the observations indicate aerosol conditions similar to those found for the reference signals (cloud-free twilight). On the contrary, if the slopes are <1 , then the observations point to the possible presence of high ALs. Note that because the high ALs increase irradiance at surface during twilight and the reference signals are plotted in the x -axis of Figure 2, the slopes are expected to be smaller than 1 under cloud conditions. In the examples illustrated in Figure 2, we obtained slope values of 1.01, 0.95, and 0.69 at 450 nm for sols 190, 178, and 311, respectively. We estimated that the slopes are significantly different to 1 when the slopes are smaller than ~ 0.97 . This threshold represents the maximum slope value below 1 for which signal differences relative to the reference signal are significant (accounting for signal errors). Therefore, based on these results we can infer that high ALs were potentially present at sunrise only for sols 178 and 311.

For determining the composition of the detected high ALs (layers made of ices or just dust), as both high-altitude clouds or detached dust layers are expected to cause similar effects on the slope values, we will make use of the ratio between the intensity at zenith measured at two different wavelengths. In particular, by choosing two wavelengths at which the single scattering albedo (or the imaginary part of the refractive index) of the dust particles is very different but approximately the same for water ice, then the value of the ratio between the intensities at these two wavelengths highly depends on the aerosol composition. We can compute these ratios, defined here as the color index (CI), from the measurements made by different RDS Top channels; a CI from the ratio between Top 3 (250–400) and Top 6 (750 nm) channels, and another CI from the ratio between Top 4 (450) and Top 6 (750 nm) channels. This selection of channels is based on the fact that dust particles have a much greater imaginary refractive index at 250–400 and 450 nm than at 750 nm (Wolff et al., 2009, 2010). According to this CI definition and since the single scattering albedo of the water (or CO_2) ice particles is ~ 1 in any of these three RDS channels, we expect greater values of Top3 (250–400 nm)/Top6 (750 nm) and Top4 (450 nm)/Top6 (750 nm) when the high-altitude ALs are made of water ice than when they are composed of only dust. Although similar results would be obtained by using the Top 8 (950 nm) channel instead of the Top 6, we made this election because the Top 6 wavelength range is the closest one to the minimum in the imaginary refractive index of the dust (Wolff et al., 2009). It is important to note here that the CI is also sensitive to variations in the cloud particle size. In particular, an increase in the particle radius of the high-altitude ALs would also decrease the CI values

(for a constant opacity). This is due to the dependence of the phase function and single scattering albedo on the particle radius.

2.3. Atmospheric and Radiative Transfer Modeling

The cloud properties are derived by modeling the RDS Top measurements with RT simulations. We first investigated the sensitivity of the RDS signals to different cloud properties (e.g., altitude, opacity, geometrical thickness, particle shape), and found that the cloud altitude, number density, and particle radius are the parameters with the greatest impact. RT simulations at twilight are made with a three-dimensional Monte Carlo RT model in spherical geometry (since the plane-parallel approximation breaks down for high SZAs) previously used for cloud properties retrievals on Earth (Gomez-Martin et al., 2021; Toledo, Rannou, Pommereau, Sarkissian, & Foujols, 2016), Titan (Rannou et al., 2016; West et al., 2016), and adapted to the Martian atmosphere (Toledo, Rannou, Pommereau, & Foujols, 2016; Toledo et al., 2017). Since Monte Carlo RT simulations take a long time to calculate, the retrieval procedure makes use of a pre-computed set of look-up tables, for minimizing the mean square difference between simulated and observed RDS signals. Cloud scattering properties are computed with Mie theory and the refractive index of water ice (Warren, 1984). The cloud geometrical thickness was fixed at 2 km (we varied this parameter up to values of 6 km and did not find significant variations in the simulations), and the cloud spatial distribution density was defined by a Gaussian height profile, scaled to produce the desired opacity. The dust scattering properties were derived from the empirical formulation proposed by Pollack and Cuzzi (1980) and using the spectral refractive index given in Wolff et al. (2009) is used. The RDS signals were normalized by the intensity measured at $\text{SZA} = 90^\circ$ (or the minimum SZA of the twilight) to reduce the impact of the background dust properties (opacity and r_{eff}) on the cloud retrievals. For the vertical distribution of dust particles, we adopted the modified Conrath profile (Conrath, 1975) proposed by Forget et al. (1999).

$$\tau(z) = \tau_0 \cdot \sigma(z) \cdot \exp\left[\nu \cdot (1 - \sigma(z)^{-1})\right] \quad (1)$$

where τ_0 is the vertical opacity at surface, $\sigma(z)$ is the ratio between the pressure at z level and the pressure at surface (here we assume p varies with height as $p = p_0 \cdot \exp(-z/H)$, where p_0 is the pressure at surface and H the scale height and equal to 11 km), ν is a constant set to 0.007 and l is the ration between a reference height (set to 70 km) and the altitude of the top of the dust layer (Z_{max}). We investigated the use of more complex dust vertical distributions in our RT simulations. Based on previous works, we simulated the RDS signals using a dust vertical profile resulting from a Conrath-type profile and a detached dust layer (defined by a Gaussian height profile) with variable altitude. We found no significant differences in the cloud retrievals using this non-monotonic dust vertical distributions for detached-dust layer altitudes less than or equal to 25 km. Based on the results reported in McCleese et al. (2010) and Heavens et al. (2011a, 2011b), which found the maximum dust mass mixing ratio at altitudes between 15 and 25 km (for MY 28–29 and for most of the northern spring and summer), we favored the simple Conrath-type profiles over more complex dust structures for our retrieval analysis.

3. Results

3.1. Presence of Clouds in the Period Ls 39°–262°

The slope analysis described in 2.2 was performed for all the twilights available up to sol 492 ($\text{Ls} = 262^\circ$), whose results are displayed in the upper panel of Figure 3a. An inspection of the slope values reveals 4 obvious periods of different high altitude aerosol activity:

1. Between $\text{Ls} \sim 39^\circ$ and 50° , high-altitude ALs signatures in the RDS signals are found for about $\sim 40\%$ of the twilights covered by MEDA. In general, the slopes obtained at sunrise are smaller than those during sunset, suggesting greater opacities or altitudes. We cannot establish the start of this period as no RDS data with high gain is available before $\text{Ls} = 39^\circ$. In the following section and in Appendix A we will show that these ALs are at altitudes above ~ 30 km.
2. The second period, between $\text{Ls} \sim 50^\circ$ and 114° , is characterized by a notable drop in the high-altitude aerosol detections: in this period, values of the slopes are close to 1. Only 27 twilights out of 101 present slopes smaller than 0.97 for Top 4 (450 nm) channel, and 15 out of 101 for Top 8 (950 nm) channel. The particular conditions which led to this decrease are unclear and will be discussed in Section 3.3.

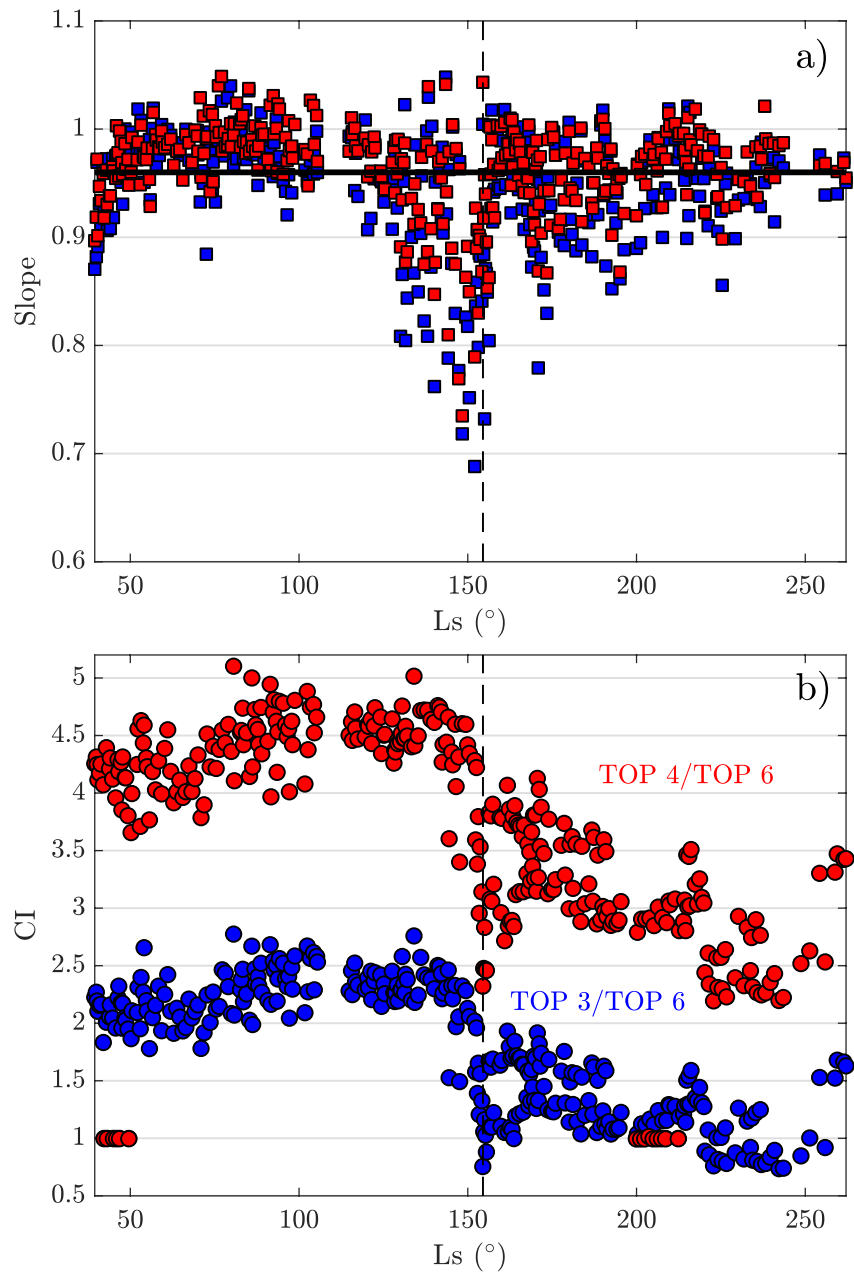


Figure 3. (a) Correlation slopes derived from the procedure described in Figure 2 and the Radiation and Dust Sensor (RDS) Top 4 (blue squares) and Top 8 (red squares) observations for the twilights covered by RDS up to sol 492. The black dashed line indicates the time when a regional dust storm was observed in Jezero (Lemmon, Smith, et al., 2022), and the black solid line shows the 0.97 threshold value. (b) color index signals used to discriminate between dust and ice are computed from the ratio between the RDS Top 3 (250–400 nm) and Top 6 (750 nm) observations (blue dots) and from the ratio between the RDS Top 4 (450) and Top 6 (750 nm) observations (red dots).

3. After the second period, we see a decrease in the slopes derived from both channels, and thus an increase in the number of twilights with the presence of high-altitude ALs. In general, the slopes during this period are smaller than those for the first period and decrease with Ls (before reaching the minimum), indicating higher aerosol altitudes or opacities if we assume that the slope in our correlation plots decrease with these two parameters (this will be demonstrated in the next section). The decrease in the correlation slopes lasts up to $L_s \sim 150^\circ$, which is when the minimum is found. During this period of maximum high-altitude aerosol activity (between $L_s = 114^\circ$ and 162°) is when the cameras of Perseverance rover and MEDA detected the

- formation of a 22° scattering halo (Lemmon, Toledo, et al., 2022) around the Sun, $L_s = 142^\circ$ and when a regional dust storm (MY36/2022A) was actively raising dust in Jezero crater (Lemmon, Smith, et al., 2022; Sánchez-Lavega et al., 2022; M. D. Smith et al., 2023), $L_s = 153^\circ$ – 156° (indicated by the black dashed line).
4. For $L_s > \sim 156^\circ$ (after the dust storm), the slopes become closer to 1 but with values smaller than during the second period and highly variable. The variability during the last period could indicate a change in the kind of aerosol (ice or dust) present in the higher parts of the atmosphere.

Although the results shown in Figure 3a may indicate a change in the aerosol-type present during twilight after the regional dust storm MY36/2022A (dashed black line in Figure 3a), from the correlation slopes we cannot directly discriminate between high-altitude detached dust layers or clouds. Indeed, in both scenarios the RDS observations at 450 and 950 nm would show an increase respect to the reference signals, and thus have a slope lower than 1 in the correlation plots. To evaluate the possible aerosol composition of the different detected high ALs, Figure 3b shows the ratios Top 3 (250–400 nm)/Top 6 (750 nm) and Top 4 (450 nm)/Top 6 (750 nm) (CI defined in Section 2.2) for the same twilights analyzed in Figure 3a. For each twilight, we represent the ratio values given at $SZA \sim 90^\circ$. From approximately $L_s = 39^\circ$ until $L_s = 150^\circ$, which is within the ACB season, the CI does not show strong variations. At the time around when the regional dust storm passed over the Perseverance rover site, the CI decreased by a factor of 2 in a few sols. This is consistent with the presence of dust layers at high altitude and the increase in the dust opacity as a result of the dust storm. Interestingly, although the CI increased once the dust storm had vanished, it never recovered the values registered before. Moreover, the CI time-series clearly shows a negative trend after $L_s \sim 172^\circ$. Therefore, based on these results we can identify two periods with different aerosol scenarios during twilight: (a) a first period from $L_s \sim 39^\circ$ to $\sim 150^\circ$ with high and stable CI values likely produced by the presence of predominantly water ice; (b) a second period with lower CI values that are decreasing with time, mainly dominated by dust. This is also consistent with the results using the observations made by MEDA-TIRS and reported in M. D. Smith et al. (2023) that a systematic change in the diurnal trend of the aerosol opacity occurred around $L_s 150^\circ$. In that work, a diurnal and a seasonal component in the aerosol opacity variability was derived, and from that it was inferred that after the regional dust storm the dust was the aerosol dominating the opacity.

On the basis of these results, we conclude that high-altitude ALs found in the correlation slopes before $L_s \sim 150^\circ$ were mainly made of ice particles, while the cases after that date corresponded to ALs whose opacity was dominated by dust. From the analysis of the correlation slopes and the CI we cannot infer whether the observed ice particles consisted of clouds (detached layers at a given altitude) or hazes vertically extended over several km. In the next section, we will make use of RT simulations to constrain the cloud properties of the detection cases before $L_s 150^\circ$. As indicated before, the CI values are also sensitive to variations in the cloud particle radius. Nonetheless, because the decrease in CI coincides with the end of the ACB season and our RT simulations do not indicate a systematic change in the particle radius around $L_s 150^\circ$, we conclude that the drop in CI is primarily due to the aerosol composition.

3.2. Cloud Altitude, Opacity, and Particle Size Retrievals

The cloud altitude, number density and particle size were derived by fitting the RDS Top 4 (450) and Top 8 (950 nm) twilight observations simultaneously with the model described in Section 2.3. The cloud opacity at each wavelength is derived from the fitted cloud number density and the particle cross section, computed from the fitted r_{eff} and the refractive index of water ice. Only the twilights for which the RDS observations covered the minimum SZA range of (91° – 97°) were considered in the analysis (a total of 161 twilights). In Appendix A we demonstrate that for clouds above ~ 30 km, our retrievals are not significantly affected by the vertical extension of the main dust layer (for this reason and to decrease the number of free parameters, our analysis is focused on altitudes above 30 km). Assuming that there were not detached dust layers above 25 km in our observations for the cloudy period, we used a $Z_{max} = 45$ km for the dust profiles. We did not find significant differences in our cloud retrievals by varying this parameter from 30 to 50 km. We also performed a sensitivity analysis for the dust opacity and r_{eff} detailed in Appendix B, to evaluate the impact of these parameters on the cloud retrievals. We found that for opacity and r_{eff} values between 0.3 and 0.6, and between 1.2 and 1.4 μm , respectively, our cloud retrievals are not significantly affected. For this reason and based on the times series of the dust opacity retrieved from images taken regularly by SkyCam (see Appendix B), these parameters are fixed to 0.4 and 1.4 μm . Regarding the cloud particle shape, we investigated the impact in the RDS signals when using different shapes other

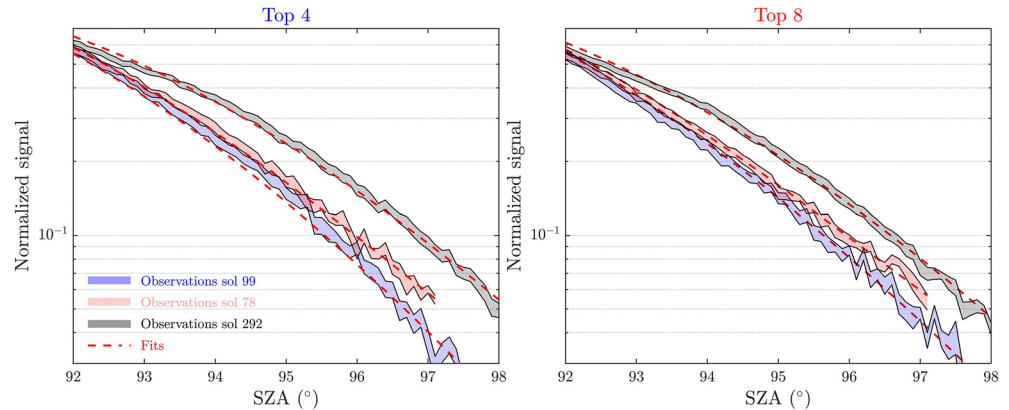


Figure 4. Comparison between simulations and observations at 450 (left) and 950 nm (right) for the twilights of sols 78, 99, and 292. The shaded areas represent the errors and the red dashed lines the simulations using the cloud parameters fitted for each case. For each twilight, the observations at 450 and 950 nm were fitted simultaneously.

than spheres (to see if adding an additional free parameter was needed). In particular, similar simulations were made but using spheroid and cylindrical particles and we did not find significant variations (see Appendix C for more information). Therefore, the only free parameters in our inversion analysis are the cloud altitude, opacity and particle radius.

Figure 4 shows three of our best fits to the data acquired by Top-4 and Top-8 sensors during twilight for sol 78, 99, and 292, and where we can see that we match the normalized signals very well (reduced Chi-square function, χ^2 , values < 1.2). For these cases, the correlation slopes are 0.97, 1.01, and 0.92 at 450 nm, and 0.96, 0.99, and 0.95 at 950 nm, respectively. For sol 99, whose slope is ~ 1 , the observations could be fitted without a cloud in the RT model. This is consistent with our assumption in Section 3.1 that slopes ~ 1 are indicative of skies free of high-altitude ALs. For the fitted signals for sol 78, whose intensities are greater than those on sol 99 for the same SZAs, we used the cloud model described above and we derived a cloud altitude, opacity and r_{eff} of 42.8 ± 4.1 km, 0.011 ± 0.004 and 1.14 ± 0.21 μm , respectively. We originally attempted to fit the data using only the dust Conrath profiles, with Z_{max} treated as a free parameter, but could not achieve a fit with a reasonably good χ^2 using this model (reduced $\chi^2 \gg 1$). However, for the same observations (sol 78), a reduced χ^2 similar to that obtained with the detached cloud model was achieved by using a cloud vertically extended over several kilometers and with $r_{eff} < 0.4$ μm . In this aerosol model, referred as the haze model thereafter, the layer of ice particles is extended over 30 km (or more) and centered at an altitude of 40 km. Therefore, for these particular observations we could not infer if the deviation with respect to the reference signals was produced by the presence of detached clouds or hazes. For the three twilights, the observations made on sol 292 show the higher deviations with respect to the reference signals, and the cloud model provides fitted cloud altitude, opacity and r_{eff} values of 42.0 ± 2.0 km, 0.031 ± 0.006 and 1.34 ± 0.52 μm , respectively. For these observations, neither the haze model nor the dust model could fit the data with a reasonably good χ^2 , thus indicating unequivocally the presence of clouds. Although the opacities derived for sol 78 and 292 are small, it is important to note that these opacities represent the average over the sensor's FOV. If, during the detection, the clouds covered only a few percent of the FOV, then our retrieved cloud opacity would be smaller than that derived from an instrument (e.g. a camera) whose FOV is fully covered by the cloud. Another point to note is that from this analysis we can only infer the cloud or haze opacity above ~ 30 km (see Appendix A), and thus the opacity contribution from clouds or hazes below this level are not included in the cloud opacity retrievals.

A similar analysis was performed for all the twilights covered by MEDA up to $L_s = 150^\circ$, which is the time when the drop in the CI is observed (Figure 3). For the complete data set (a total of 161 twilights analyzed with the RT model), the signals shown in Figure 4 are representative examples. In 54 twilights, RDS observations indicated the presence of clouds, whose fitted parameters are displayed in the left panels of Figure 5 (a, c, and e). In these cases, the cloud model achieved reduced χ^2 values < 1.2, and similar results were not obtained (in terms of χ^2) by replacing the cloud layer by a vertically extended haze. That is to say, these cases are like the twilight on sol 292 analyzed in Figure 4. On the other hand, for a total of 40 twilights, we found that both the cloud and haze models fitted the data with reduced χ^2 values < 1.2. The results obtained for these cases using the cloud model

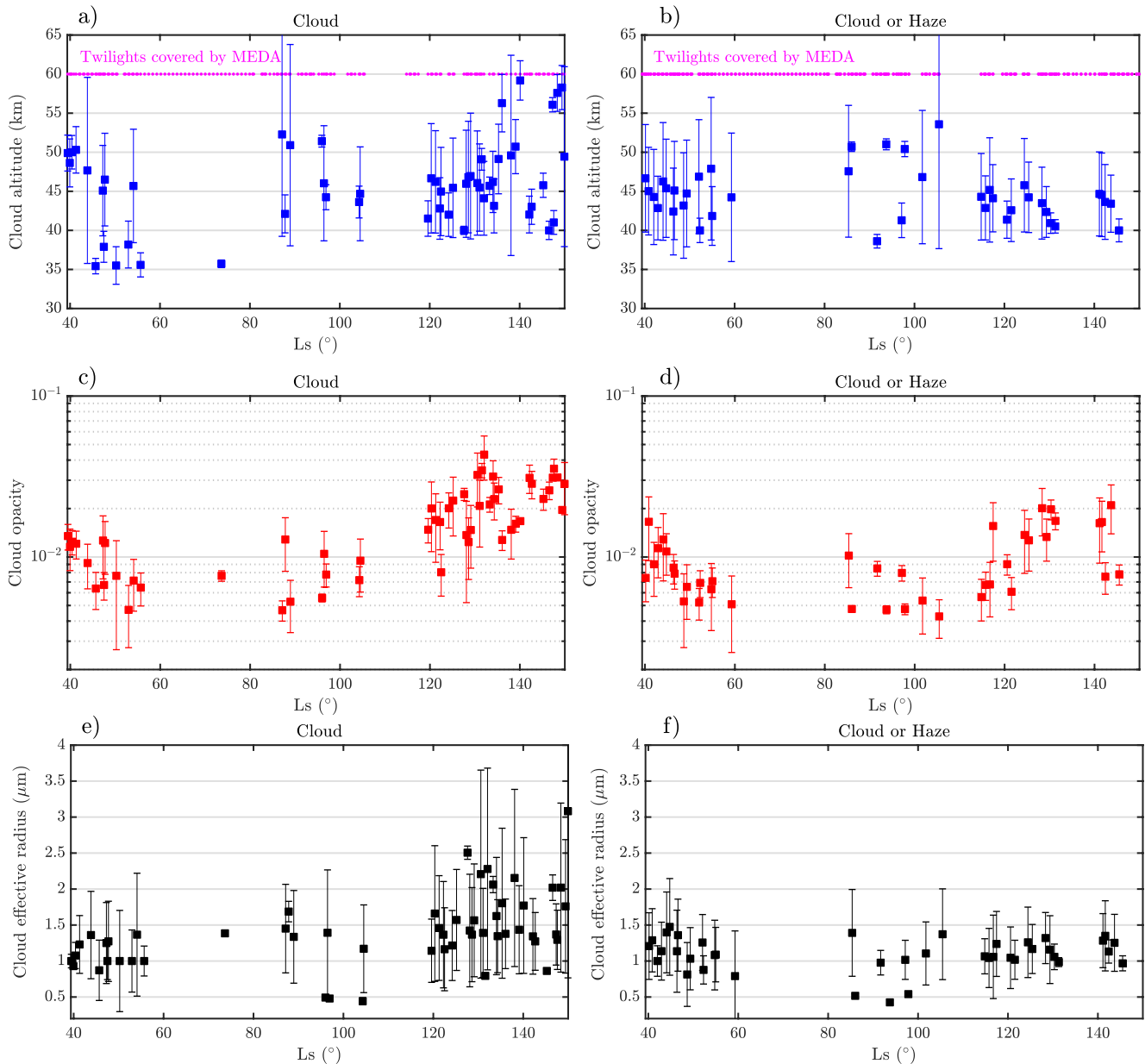


Figure 5. Cloud altitude, opacity, and effective radius (r_{eff}) retrieved from Radiation and Dust Sensor (RDS) Top-4 and Top-8 twilight observations up to $L_s = 150^\circ$ using the cloud model described in Section 2.3. The left panels (a, c, and e) represent the cloud cases for which only the cloud model could fit the data with a reduced $\chi^2 < 1.2$, while the right ones (b, d, and f) the cases for which both the cloud and haze models achieved fits with reduced $\chi^2 < 1.2$. The purple dots indicate the twilight L_s dates for which the minimum solar zenith angles range (91° – 97°) was covered by the RDS observations.

are displayed in the right panels of Figure 5 (b, d, and f). For the rest of the twilights, we have: (a) 42 cases with cloud opacities below our limit of detection (~ 0.004), defined in this work as the minimum opacity to produce a variation of at least 5% respect to the reference signals at $SZA = 93^\circ$; (b) 25 cases for which none of the models achieved a good fit (likely due to changes in the cloud opacity during the twilight period or to complex aerosol scenarios). Therefore, in the 58% of the twilights analyzed we found signatures of clouds or hazes in the RDS signals. In most of the cases the clouds were found at altitudes between 40 and 50 km. Based on these altitudes, we assume these clouds are made of water ice. However, we point that from the modeling of the RDS signals, we cannot directly discriminate between clouds made of CO_2 or H_2O ice. Therefore, we can not rule out the possibility that some of the clouds shown in Figure 5 are made of CO_2 ice (in particular those with the highest altitudes). In general, the cloud particle sizes were in the range between $r_{eff} = 0.6$ and $2 \mu m$ (accounting for the errors in this

parameter), which is in agreement with the sizes derived in previous works (e.g., Guzewich & Smith, 2019) from orbital observations.

Similar to the results shown in Figure 3, the cloud and haze retrievals show an increase in the cloud opacity in the period between $L_s \sim 120^\circ$ and 150° , which is when the scattering halo was observed (Lemmon, Toledo, et al., 2022). The minimum and maximum cloud opacities registered for this period are 0.008 ± 0.002 and 0.043 ± 0.013 , which again represent the average cloud opacity over the RDS Top sensors FOV. We also see a decrease in the number of cloud and haze detections in the period between $L_s \sim 50^\circ$ and 114° , as well as a decrease in the cloud altitude and opacity, which confirms the conclusions derived in previous section from the correlation slope analysis; within the ACB season and assuming the cloudy season started in Jezero at $L_s \sim 39^\circ$ or before, the RDS twilight observations point to a discontinuity in the cloud activity above ~ 30 km around aphelion ($L_s \sim 70^\circ$). In general, observations made by the Visual Monitoring Camera (VMC) camera aboard Mars Express along MYs 29 to 35 show a low presence of twilight clouds at the latitude of Jezero crater compared to latitudes farther south (Hernández-Bernal et al., 2021). A comparison of both methods suggests that with RDS we easily detect morning and evening clouds or hazes of low optical thickness while from orbit we detect clouds with much higher optical thicknesses.

3.3. The Decrease in Cloud Activity Around $L_s 70^\circ$

The results discussed in previous sections indicate a notable decrease in the cloud activity, opacity and height for the period around aphelion ($L_s = 70^\circ$). This particular seasonal feature of the cloud distribution has been observed in some previous datasets. Hernández-Bernal et al. (2021) investigated the formation of clouds in the mesosphere using images from the Mars Express VMC camera at twilight, and found a decrease in the cloud activity around the same period. However, this particular seasonal variation does not appear to be present in orbiter-derived records of water ice column opacity ($\tau_{ice-column}$). For instance, the data set of $\tau_{ice-column}$ for more than 3.5 MY derived in M. D. Smith (2009) from THEMIS instrument on-board Mars Odyssey does not appear to show a minimum in $\tau_{ice-column}$ for $L_s \sim 70^\circ$. Similar conclusions are drawn from the $\tau_{ice-column}$ values derived in Wolff et al. (2022) and Atwood et al. (2022) from observations by instruments on-board the Emirates Mars Mission. For the same period analyzed in this work, the column aerosol optical depth (dust plus water ice cloud) derived in M. D. Smith et al. (2023) from MEDA-TIRS observations does not display a minimum around aphelion either. A possible explanation for these different results is that the decrease in cloud activity around aphelion occurs only at altitudes above 30–35 km for which the cloud opacity (Figure 5) is very small compared to $\tau_{ice-column}$. M. D. Smith et al. (2023) demonstrated that up to $L_s = 150^\circ$, ice is the aerosol component dominating the diurnal and seasonal variability of the aerosol optical depth in Jezero. These variations can be as large as 0.2, which is roughly 10 times greater than the largest cloud opacity retrieved in this study. If the mesospheric-cloud opacities represent this small percentage of $\tau_{ice-column}$, then it would be difficult to detect the seasonal variations reported in this study using such measurements. Therefore, the fact that the minimum around aphelion reported in this work is not found in $\tau_{ice-column}$ indicates that this particular seasonal feature occurs only at altitudes above 30–35 km. Interestingly, the decrease in mesospheric-cloud activity around aphelion has also been reported for CO_2 clouds. Using observations at limb from the Thermal Emission Spectrometer and the Mars Orbiter Camera onboard the Mars Global Surveyor, Clancy et al. (2003, 2007) reported the occurrence of equatorial mesospheric clouds during MYs 24–26. The seasonal variation of detections revealed a first period of mesospheric cloud activity between $L_s = 0^\circ$ and 55° , a pause in cloud occurrence around aphelion, and a second period of cloud activity between $L_s = 105^\circ$ and 180° . A similar decrease in the equatorial mesospheric cloud activity around aphelion (in particular between $L_s = 60^\circ$ and 90° , see Määttä et al. (2013)) was also revealed from the spectrometer OMEGA on board Mars Express.

The decrease in the cloud activity around aphelion reported in Figures 3 and 5 can be mainly due to variations in: (a) the saturation ratio (S), defined as the ratio of the partial pressure of the vapor to its saturation vapor pressure and (b) the concentration of cloud condensation nuclei (dust particles). A decrease in S can be produced by a decrease in the partial pressure of water or by an increase in the saturation vapor pressure. The saturation vapor pressure decreases with decreasing temperature. A decrease in S resulting from rising temperature is not expected for $L_s \sim 70^\circ$ (based on modeling as we will show below).

With regard to the concentration of condensation nuclei, the seasonal variability of the vertical extension of the main dust layer may have an impact on the cloud activity reported here. From the analysis of stellar occultations

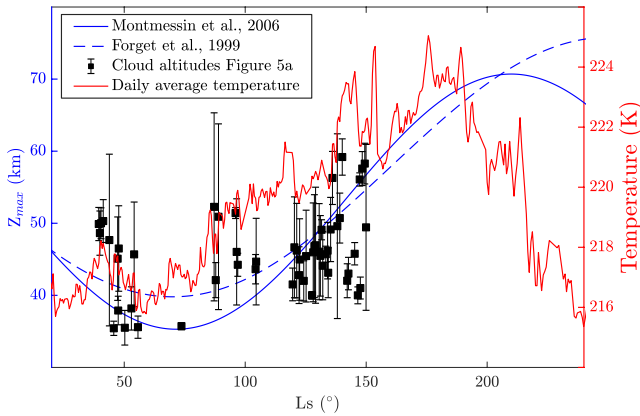


Figure 6. Variation of the haze top with Ls given in Montmessin et al. (2006) (blue solid line) and Forget et al. (1999) (blue dashed line), along with the daily average temperature (red solid line, right y-axis). For comparison purposes, the cloud altitudes derived in this work are also displayed.

at UV wavelengths by the SPICAM instrument, Montmessin et al. (2006) derived the seasonal variations of the top of the haze layer (Z_{\max}^{haze}), and found a correlation with the eccentric Martian orbit. In particular, in that work the altitude of the haze layer top was fitted to a cosine function, whose minimum (hazetop minimum) occurs near aphelion. On the basis of the dust climatology reported in Anderson and Leovy (1978) and Jaquin et al. (1986), who also found a link between Z_{\max}^{haze} and the variable insolation driven by the orbit eccentricity, Forget et al. (1999) derived the function $60 + 18 \cdot \sin(Ls - 160^\circ) - 22 \cdot \sin(\phi)^2$, where ϕ is the latitude, to parametrize the seasonal variation of the altitude of the top of the dust layers. Figure 6 shows the variation of Z_{\max}^{haze} with Ls given by the functions reported in both works, along with the daily average temperature at 1.45 m derived from the MEDA-ATS and the procedure described in Munguira et al. (2022). Here we see that both works report the minimum in the dust vertical extension during aphelion (at $Ls \sim 70^\circ$). As discussed in Montmessin et al. (2006), the minimum in Z_{\max}^{haze} during this period (minimum in temperatures) results from the weakening of convective activity and the lower altitude of the cloud condensation level (dust scavenging by the clouds at the condensation level limits the amount of dust that can be transported to upper altitudes). This scenario could explain the minimum

in the cloud activity at altitudes above ~ 30 km found in this work since a notable decrease in the concentration of dust particles (cloud nuclei) in the mesosphere could inhibit the formation of clouds.

Another potential reason for the decrease in the cloud activity is the seasonal variation of the water vapor. We compared our results with the output of the Mars Climate Database (MCD) developed at the Laboratoire de Météorologie Dynamique (Forget et al., 1999). Figure 7 shows MCD outputs of the water vapor volume mixing ratio (n_{H_2O}) and water ice mixing ratio (τ_{ice}) in Jezero at 6.0 hr local time for Ls between 40° and 100° and at altitudes between 20 and 50 km. These simulations are given for the average dust climatology scenario; see Madeleine et al. (2011) and Navarro et al. (2014) for a full description of the model including the dust and water cycles. From these MCD outputs we identify a decrease in n_{H_2O} around aphelion at altitudes above 30 km, displaying the greatest drop between $Ls = 40^\circ$ and 50° and at altitudes above ~ 30 km. Although the drop in the cloud activity shown in Figure 5 occurs after $Ls \sim 50^\circ$, the n_{H_2O} profiles indicate a minimum around aphelion. We also see that the τ_{ice} profiles shown in Figure 7 indicate a minimum around the same period and at altitudes above ~ 30 km, which is consistent with the results reported in this work.

In summary we find that the decrease in the cloud activity around $Ls 70^\circ$ can be explained by: (a) the expected lower altitudes of the top of the dust layer because of the weakening of the convective activity; (b) the lower altitude of the cloud condensation level; and (c) the seasonal variation of n_{H_2O} (MCD predicts lower values around aphelion). The total column opacity derived from orbiter and ground-based observations does not show a minimum around that period. This suggests that the decrease in the cloud activity found in this work must occur only at altitudes above 30–35 km. We compared our results with the water ice cloud occurrence and properties derived in Stcherbinine et al. (2022) from solar occultation measurements by the atmospheric chemistry suite

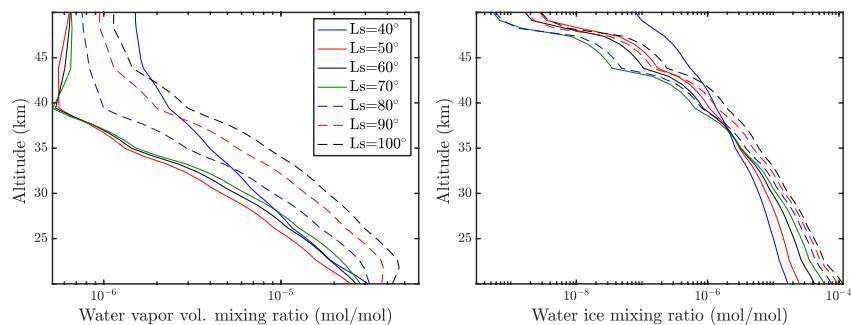


Figure 7. Mars Climate Database results: variation of water vapor vol. mixing ratio (mol/mol) (left) and water ice mixing ratio (mol/mol) (right) with Ls and altitude at Perseverance landing location (longitude 77.45°E and latitude 18.44°N).

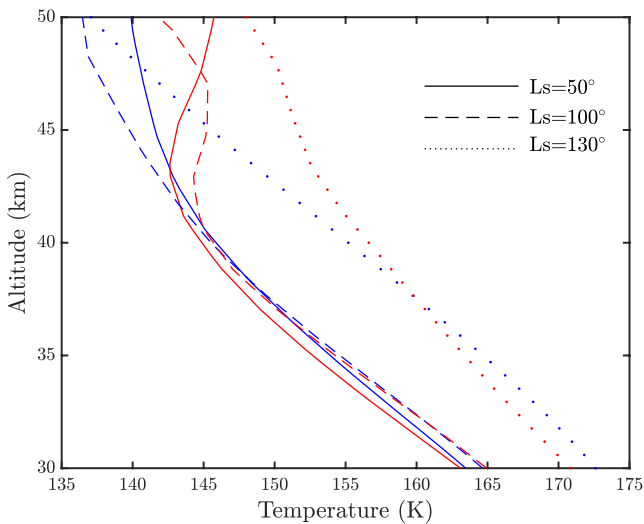


Figure 8. Mars Climate Database results: variation of temperature with altitude at sunrise (blue lines) and sunset (red lines) at three different Ls: 50° (solid lines), 100° (dashed lines), and 130° (dotted lines). These simulations are for the average dust climatology scenario and at Perseverance landing location.

instrument on-board the ExoMars Trace Gas Orbiter (from Ls = 163° MY 34 to Ls = 181° MY 36). The cloud retrievals reported in that work do not show a pause in the cloud occurrence similar to that found here. Figure 1 of Scherbinine et al. (2022) shows that there is no temporal coverage near aphelion at latitudes close to the equator (for the observations used in that study). Therefore, we conclude that a latitudinal component may be present in the cloud activity above 30–35 km.

3.4. Cloud Activity During Sunrise and Sunset

As indicated above, in 58% of the twilights analyzed with the RT simulations (a total of 161 twilights) in Ls 39°–150° we found signatures of clouds or hazes in the RDS signals. In the 65% of the sunrises (with a total of 77 cases) we have positive detections, while for the sunsets (with 84 cases) this is 52%. This different number of detections is likely due to the lower temperatures during the sunrise period. From MEDA-ATS observations, we found the minimum temperatures at sunrise to be about ~20° cooler than at sunset (at surface). If temperatures are also greater at sunset at the altitudes analyzed in this work (although not necessarily with the same difference as at surface), then we might expect a greater saturation vapor pressure during sunset, and thus higher the partial pressure of the water vapor needed to reach the saturation. This is consistent with the temperature predicted by the MCD.

Figure 8 shows the temperatures profiles at sunrise and sunset predicted by MCD at three different Ls during the cloudy season. Here we see warmer temperatures at sunset compared with sunrise at altitudes higher than ~40 km, which would explain the differences in the cloud frequency of formation in these two periods. For the detection cases shown in Figure 5, we found cloud altitudes around 47 ± 4 at sunrise and of 43 ± 5 km at sunset. Although from the temperature profiles displayed in Figure 8 we might expect clouds to form at higher altitudes at sunset rather than at sunrise, it is important to note here that, as a result of the errors in the estimation of the cloud altitude, we cannot establish if these model-determined differences in cloud altitude at sunrise and sunset are significant. Another factor that might bias the comparison between sunrise and sunset cloud altitudes is the seasonal variability of this parameter and the sampling of sunrises and sunsets covered by RDS, which is not always the same. The same applies to the cloud opacity and particle radius. Thus, except for the cloud activity, we cannot establish whether or not the cloud parameters are significantly different between these two periods.

4. Conclusions

In this paper we have presented the first analysis of the MEDA-RDS observations made during twilight for the first 492 sols of the mission. We have demonstrated the capability of these observations to detect and characterize clouds (altitude, opacity and particle radius) above ~30 km at the Perseverance landing site. We reached the following main conclusions:

1. The RDS observations indicate high-altitude ALs present at twilight during the analyzed period Ls 39°–262° (although the first sol of the mission is for Ls 6°, the RDS measurements with an appropriate gain for this study were not available until Ls 39°). Based on the CI values, we infer the main constituent of these ALs to be ice for Ls < ~150° (during the ACB season) or dust for Ls > ~150°. The time of this change in the aerosol composition is almost coincident with the regional dust storm that developed around Ls ~ 153° (Lemmon, Smith, et al., 2022; Sánchez-Lavega et al., 2022) and which was also observed by orbiter instrumentation such as the Emirates Mars Infrared Spectrometer (M. D. Smith et al., 2022) or the Mars Climate Sounder (MCS) (see MCS dust maps in http://www-mars.lmd.jussieu.fr/mars/dust_climatology/index.html described in Montabone et al. (2020)).
2. For the cloudy period, Ls 39°–150°, our RT simulations show the presence of clouds or hazes for 58% of the twilights analyzed (a total of 161), or for 65% and 52% of the sunrises and sunsets covered by RDS, respectively. The higher cloud activity during sunrise is likely due to the lower temperatures compared sunset. For the rest of the twilights covered by RDS, our model provided cloud opacities below our limit of detection

- (42 cases) or could not fit the data reasonably well (reduced χ^2 values > 1.2) (25 cases). These latter cases are probably due to changes in the cloud opacity during the twilight period (~ 30 min) or to complex aerosol vertical distributions not reproduced by the model.
- From the slopes of the correlation analysis and the RT retrievals, a notable decrease in cloud activity is identified in the period Ls 50° – 114° , around aphelion, which is approximately when the MEDA-ATS sensors report the minimum temperatures at surface. From the few detection cases, we also see for this period a decrease in the cloud altitude and opacity. The column cloud aerosol optical depth (dust plus water ice) reported in M. D. Smith et al. (2023) at the same location and time does not show a minimum at the same period, nor do the water ice column opacities ($\tau_{ice-column}$) derived from orbiter observations. This indicates that the reduced cloud activity observed in this work is occurring at altitudes above 30–35 km but not below, and that, as a result of the small opacities given in Figure 5 with respect to $\tau_{ice-column}$, the decrease in cloud activity at Ls $\sim 70^\circ$ is not evident in such measurements.
 - Less cloud activity (above 30–35 km) during the aphelion was also found in previous years (e.g., Hernández-Bernal et al., 2021) over the equator and the southern belt around 45° S, which might indicate this is a seasonal feature. Based on previous analyses and the predictions by the MCD model, we infer these variations in the cloud activity might be due to a decrease in the concentration of the cloud nuclei (dust particles) or in the water vapor mixing ratio in the mesosphere.
 - The cloudiest time over the Perseverance site for the analyzed period is between Ls = 120° – 150° for which we also find the greatest cloud opacities (maximum value 0.04 ± 0.01 weighted over the RDS Top sensors FOV). For the whole cloudy period, we found an average cloud altitude and opacity of 46 ± 4 km and 0.017 ± 0.004 , respectively. In most of the cases, the cloud particles sizes (effective radius) were found to be in between 0.6 and 2 μ m. Based on the retrieved cloud altitudes and the analyzed period (ACB period), we infer that the detected clouds are made of H₂O ice. However, from the RDS observations is not possible to directly discriminate between CO₂ or H₂O ice particles, and thus we cannot rule out the possibility that some of the detected cloud layers were made of CO₂. Interestingly, the seasonal variation in cloud activity reported in this work is similar to that reported in previous works for the equatorial CO₂ ice clouds (Määttä et al., 2013).

Appendix A: Vertical Extension of the Dust Layer

In the aerosol model described in Section 2.3 we have assumed a constant altitude of the main dust layer, parametrized with Z_{max} in the Conrath profiles (Equation 1), and equal to 45 km based on previous works (Forget et al., 1999; Montmessin et al., 2006). To investigate the impact of using a constant value of this parameter on the cloud retrievals, we varied Z_{max} from 45 to 35 km in our simulations. Figure A1 shows the variation of RDS Top-8 signal with SZA for different cloud altitudes and Z_{max} . For a cloud altitude of 20 km (left top panel), we see that the election of Z_{max} has a significant impact on the simulated signals. This is because above the cloud layer (in this particular case above 20 km), there is still a significant dust opacity affecting the irradiance observations. However, we see that as the cloud altitude is higher, the impact of Z_{max} on the simulated signals is smaller. That is to say, the cloud altitude at which above it the dust opacity is not significant, establishes the altitude at which Z_{max} does not have an impact on the retrievals. From the simulations shown in Figure A1, we see that the cases with cloud altitudes below 30–35 km are affected by Z_{max} , and thus those cases are not considered in the analysis. We could treat Z_{max} as a free parameter in our retrievals (and so include cases with cloud altitudes below 30–35 km), but then our model would be highly degenerate (multiple solutions). For this reason, our analysis is limited to clouds with altitudes above 30 km.

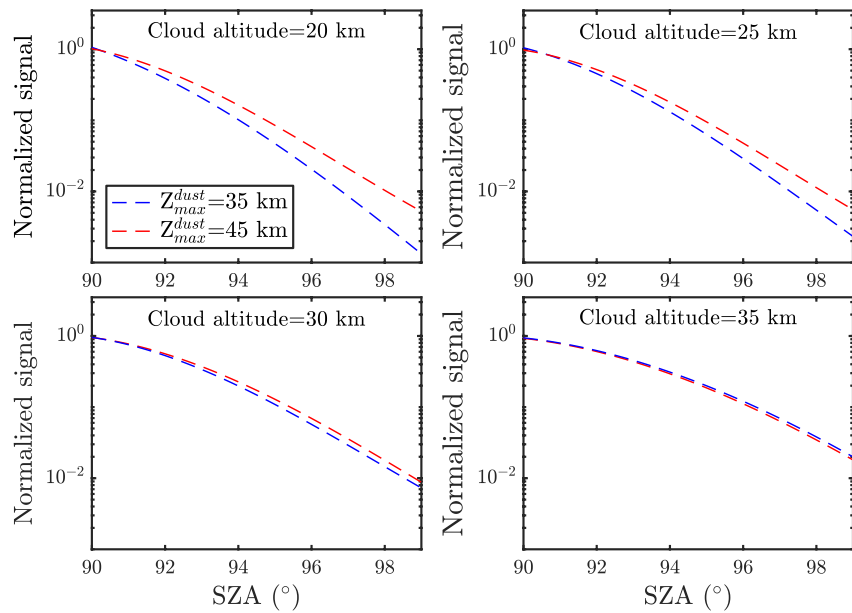


Figure A1. Radiation and Dust Sensor Top signals at 950 nm simulated for $Z_{max} = 35$ km (blue dashed line) and 45 km (red dashed line), and different cloud altitudes: 20, 25, 30, and 35 km. The dust optical properties are the same as in Figure 4.

Appendix B: Dust Opacity and Particle Radius

The retrieval analysis of the cloud properties is made for constant values of the dust opacity and r_{eff} . This election was made attending to: (a) a number of RT simulations of the RDS signals for different values of these parameters; (b) the expected values of these parameters during the cloudy season; and (c) the increase in the degeneracy of our model when adding multiple free parameters. Figure B1 shows, as example, RDS Top-8 signals simulated for different dust opacities and dust effective radii. While for the dust r_{eff} we find similar results, we see that for dust opacities smaller than ~ 0.3 or greater than ~ 0.6 the differences respect to the nominal case can be significant. Figure B2 shows the times series of the dust opacity retrieved from images taken regularly by SkyCam. These measurements are for the morning or the afternoon, and if two opacities are available for the same day, then the average of the two is represented. Except for a few cases (indicated with purple squares), the aerosol opacity was within the range (0.3–0.6). Therefore, except for these cases we do not expect larger systematic errors in the cloud retrievals caused by our assumptions of constant dust opacity and particle radius.

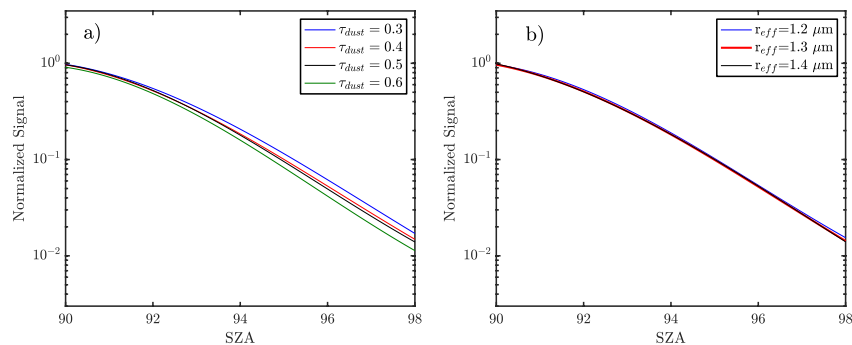


Figure B1. Radiation and Dust Sensor Top signals at 950 nm simulated for: (a) different dust opacities and a constant r_{eff} of 1.4 μm (left); (b) different dust effective radii and a constant dust opacity of 0.4 (right). In all the simulations a cloud layer is set at 40 km.

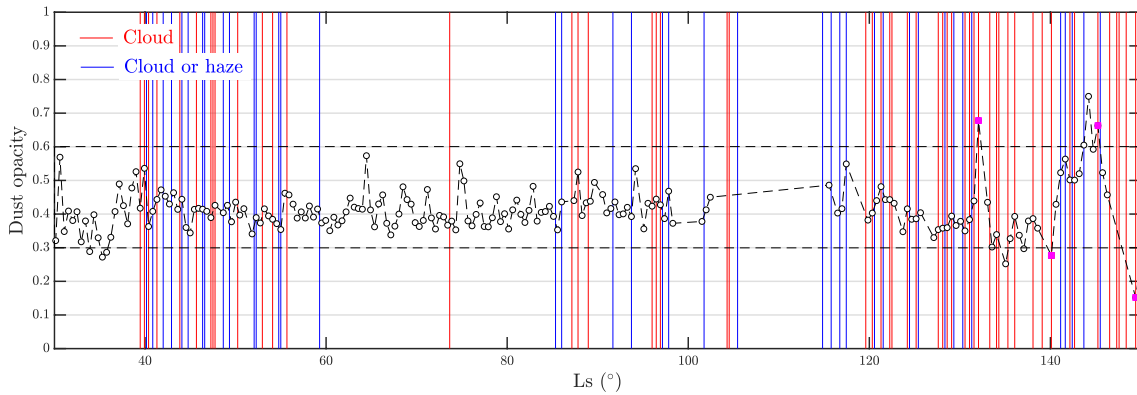


Figure B2. AO derived from the images taken regularly by SkyCam in the morning or afternoon. If for a single day two AO measurements are available, then the average of the two is represented. The red and blue lines indicate the cloud and cloud-or-haze detection cases, respectively. The cases for which the AO was not in the range 0.3–0.6 (black dashed lines) are indicated with the purple squares.

Appendix C: Cloud Particle Shape

In Section 3.2 we have assumed that the scattering properties of clouds can be modeled using spherical particles (or Mie theory). However, cloud particles made of water ice may present more complex shapes, and thus the errors induced by assuming spherical particles should be evaluated. To this end, we computed different phase functions using the T-Matrix approach (Mishchenko, 1991; Mishchenko & Travis, 1994) for spheroid and cylindrical particles with different aspect ratios (ϵ). For spheroids, ϵ is the ratio of the horizontal to the rotational semi-axes, while for cylinders ϵ is the diameter-to-length ratio. Figure C1 shows the phase functions for spheroid and cylindrical particles with different values of ϵ , an r_{eff} of 1 μm (in terms of the surface-equivalent-sphere radius) and the refractive index of water ice. Using these different phase functions, we simulated the RDS Top-8 observations for a cloud at an altitude of 40 km and an opacity of 0.005. The simulated signals are displayed in Figure 5 for which we used the same dust model as in Figure 4. Here we see that the cloud particle shape does not have a major impact on the simulated signals, with differences respect to the signal for spherical particles smaller than 5% at $\text{SZA} = 93^\circ$. This is explain by the broad FOV of the RDS Top sensors ($\pm 15^\circ$ in zenith angle). For a constant SZA, the RDS Top-8 and Top-4 sensors receive light at scattering angles between $\text{SZA} - 15^\circ$ and $\text{SZA} + 15^\circ$. Thus, our observations are mainly sensitive to the angles of the phase function in the range $\text{SZA} \pm 15^\circ$, smoothing the differences produced by the different particle shapes.

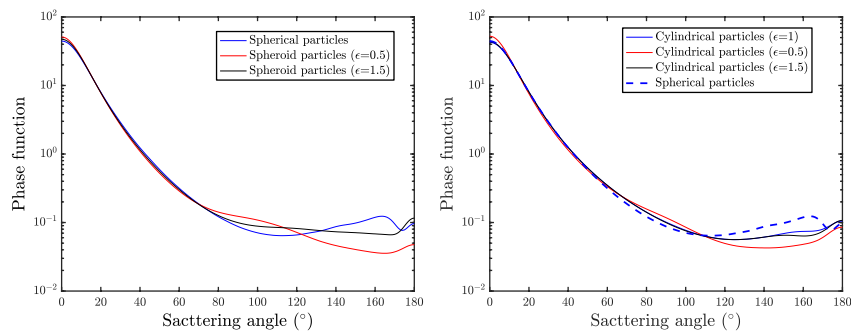


Figure C1. Phase functions at 950 nm computed with T-Matrix for spheroid (left) and cylindrical (right) particles with different aspect ratios. These phase functions are for particles with r_{eff} of 1 μm and the refractive index of water ice.

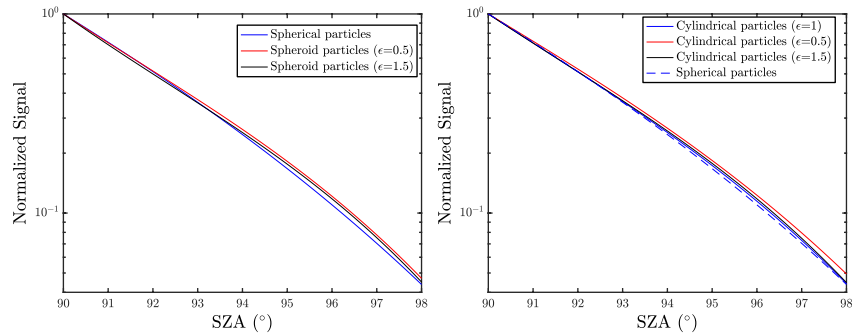


Figure C2. Radiation and Dust Sensor Top-8 signals simulated for a cloud layer at an altitude of 40 km and opacity of 0.005, and the phase functions illustrated in Figure C1. For the dust particles, we used the model described in Section 2.3 (or in Figure 4).

Data Availability Statement

All Perseverance data used in this study are publicly available via the Planetary Data System (Rodríguez-Manfredi & de la Torre Juárez, 2021). The slope and CI analyses, radiative transfer simulations, cloud retrievals, temperatures, and MCD data of Figures 1–8, A1, B1, B2, C1, and C2 are available in an archive located at Toledo (2023).

Acknowledgments

This work has been funded by the Spanish Ministry of Economy and Competitiveness, through the projects no. ESP2014-54256-C4-1-R (also ESP2014-54256-C4-2-R, ESP2014-54256-C4-3-R, and ESP2014-54256-C4-4-R), Spanish Ministry of Science, Innovation and Universities, projects no. ESP2016-79612-C3-1-R (also ESP2016-79612-C3-2-R and ESP2016-79612-C3-3-R), Spanish Ministry of Science and Innovation/State Agency of Research (10.13039/501100011033), projects no. PID2021-126719OB-C41, ESP2016-80320-C2-1-R, RTI2018-098728-B-C31 (also RTI2018-098728-B-C32 and RTI2018-098728-B-C33), RTI2018-099825-B-C31. RH and ASL were supported by the Spanish project PID2019-109467GB-I00 funded by MCIN/AEI/10.13039/50110001103 and by Grupos Gobierno Vasco IT1742-22. The US co-authors performed their work under sponsorship from NASA's Mars 2020 project, from the Game Changing Development programme within the Space Technology Mission Directorate and from the Human Exploration and Operations Directorate. Part of this research was carried out at the Jet Propulsion Laboratory, California Institute of Technology, under a contract with the National Aeronautics and Space Administration (80NM0018D0004). G.M. acknowledges JPL funding from USRA Contract Number 1638782. ML is supported by contract 15-712 from Arizona State University and 1607215 from Caltech-JPL. A. V-R. is supported by the Comunidad de Madrid Project S2018/NMT-4291 (TEC2SPACE-CM).

References

- Anderson, E., & Leovy, C. (1978). Mariner 9 television limb observations of dust and ice hazes on Mars. *Journal of the Atmospheric Sciences*, 35(4), 723–734. [https://doi.org/10.1175/1520-0469\(1978\)035<0723:mtlood>2.0.co;2](https://doi.org/10.1175/1520-0469(1978)035<0723:mtlood>2.0.co;2)
- Apestigue, V., Gonzalo, A., Jiménez, J. J., Boland, J., Lemmon, M., de Mingo, J. R., et al. (2022). Radiation and dust sensor for Mars environmental dynamic analyzer onboard M2020 rover. *Sensors*, 22(8), 2907. <https://doi.org/10.3390/s22082907>
- Atwood, S. A., Smith, M. D., Badri, K., Edwards, C. S., Christensen, P. R., Wolff, M. J., et al. (2022). Diurnal variability in emirs daytime observations of water ice clouds during Mars aphelion-season. *Geophysical Research Letters*, 49(15), e2022GL099654. <https://doi.org/10.1029/2022gl099654>
- Benson, J. L., Kass, D. M., & Kleinböhl, A. (2011). Mars' north polar hood as observed by the Mars climate sounder. *Journal of Geophysical Research*, 116(E3), E03008. <https://doi.org/10.1029/2010je003693>
- Benson, J. L., Kass, D. M., Kleinböhl, A., McCleese, D. J., Schofield, J. T., & Taylor, F. W. (2010). Mars' south polar hood as observed by the Mars climate sounder. *Journal of Geophysical Research*, 115(E12), E12015. <https://doi.org/10.1029/2009je003554>
- Clancy, R. T., Grossman, A., Wolff, M., James, P., Rudy, D., Billawala, Y., et al. (1996). Water vapor saturation at low altitudes around Mars aphelion: A key to Mars climate? *Icarus*, 122(1), 36–62. <https://doi.org/10.1006/icar.1996.0108>
- Clancy, R. T., Wolff, M. J., & Christensen, P. R. (2003). Mars aerosol studies with the MGS TES emission phase function observations: Optical depths, particle sizes, and ice cloud types versus latitude and solar longitude. *Journal of Geophysical Research*, 108(E9), 5098. <https://doi.org/10.1029/2003je002058>
- Clancy, R. T., Wolff, M. J., Whitney, B. A., Cantor, B. A., & Smith, M. D. (2007). Mars equatorial mesospheric clouds: Global occurrence and physical properties from Mars global surveyor thermal emission spectrometer and Mars orbiter camera limb observations. *Journal of Geophysical Research*, 112(E4), E04004. <https://doi.org/10.1029/2006je002805>
- Conrath, B. J. (1975). Thermal structure of the Martian atmosphere during the dissipation of the dust storm of 1971. *Icarus*, 24(1), 36–46. [https://doi.org/10.1016/0019-1035\(75\)90156-6](https://doi.org/10.1016/0019-1035(75)90156-6)
- Fedorova, A. A., Montmessin, F., Korabiev, O., Luginin, M., Trokhimovskiy, A., Belyaev, D. A., et al. (2020). Stormy water on Mars: The distribution and saturation of atmospheric water during the dusty season. *Science*, 367(6475), 297–300. <https://doi.org/10.1126/science.aay9522>
- Forget, F., Hourdin, F., Fournier, R., Hourdin, C., Talagrand, O., Collins, M., et al. (1999). Improved general circulation models of the Martian atmosphere from the surface to above 80 km. *Journal of Geophysical Research*, 104(E10), 24155–24175. <https://doi.org/10.1029/1999je001025>
- Forget, F., & Pierrehumbert, R. T. (1997). Warming early Mars with carbon dioxide clouds that scatter infrared radiation. *Science*, 278(5341), 1273–1276. <https://doi.org/10.1126/science.278.5341.1273>
- Giuranna, M., Wolkenberg, P., Grassi, D., Aronica, A., Aoki, S., Scaccabarozzi, D., et al. (2021). The current weather and climate of Mars: 12 years of atmospheric monitoring by the planetary Fourier spectrometer on Mars express. *Icarus*, 353, 113406. <https://doi.org/10.1016/j.icarus.2019.113406>
- Gomez-Martín, L., Toledo, D., Prados-Roman, C., Adame, J. A., Ochoa, H., & Yela, M. (2021). Polar stratospheric clouds detection at Belgrano ii Antarctic station with visible ground-based spectroscopic measurements. *Remote Sensing*, 13(8), 1412. <https://doi.org/10.3390/rs13081412>
- Guzewich, S. D., & Smith, M. (2019). Seasonal variation in Martian water ice cloud particle size. *Journal of Geophysical Research: Planets*, 124(2), 636–643. <https://doi.org/10.1029/2018je005843>
- Heavens, N., Richardson, M., Kleinböhl, A., Kass, D., McCleese, D., Abdou, W., et al. (2011a). Vertical distribution of dust in the Martian atmosphere during northern spring and summer: High-altitude tropical dust maximum at northern summer solstice. *Journal of Geophysical Research*, 116(E1), E01007. <https://doi.org/10.1029/2010je003692>
- Heavens, N., Richardson, M., Kleinböhl, A., Kass, D., McCleese, D., Abdou, W., et al. (2011b). The vertical distribution of dust in the Martian atmosphere during northern spring and summer: Observations by the Mars climate sounder and analysis of zonal average vertical dust profiles. *Journal of Geophysical Research*, 116(E4), E04003. <https://doi.org/10.1029/2010je003691>

- Hernández-Bernal, J., Sánchez-Lavega, A., del Río-Gaztelurrutia, T., Hueso, R., Ravanis, E., Cardesín-Moinelo, A., et al. (2021). A long-term study of Mars mesospheric clouds seen at twilight based on Mars express VMC images. *Geophysical Research Letters*, 48(7), e2020GL092188. <https://doi.org/10.1029/2020GL092188>
- Jaquin, F., Gierasch, P., & Kahn, R. (1986). The vertical structure of limb hazes in the Martian atmosphere. *Icarus*, 68(3), 442–461. [https://doi.org/10.1016/0019-1035\(86\)90050-3](https://doi.org/10.1016/0019-1035(86)90050-3)
- Lemmon, M. T., Smith, M. D., Viudez-Moreiras, D., de la Torre-Juarez, M., Vicente-Retortillo, A., Munguira, A., et al. (2022). Dust, sand, and winds within an active Martian storm in Jezero Crater. *Geophysical Research Letters*, 49(17), e2022GL100126. <https://doi.org/10.1029/2022gl100126>
- Lemmon, M. T., Toledo, D., Apestigue, V., Arruego, I., Wolff, M. J., Patel, P., et al. (2022). Hexagonal prisms form in water-ice clouds on Mars, producing halo displays seen by perseverance rover. *Geophysical Research Letters*, 49(17), e2022GL099776. <https://doi.org/10.1029/2022gl099776>
- Lemmon, M. T., Wolff, M. J., Bell, J. F., III, Smith, M. D., Cantor, B. A., & Smith, P. H. (2015). Dust aerosol, clouds, and the atmospheric optical depth record over 5 Mars years of the Mars exploration rover mission. *Icarus*, 251, 96–111. <https://doi.org/10.1016/j.icarus.2014.03.029>
- Lorenz, R. D., Lemmon, M. T., Maki, J., Banfield, D., Spiga, A., Charalambous, C., et al. (2020). Scientific observations with the insight solar arrays: Dust, clouds, and eclipses on Mars. *Earth and Space Science*, 7(5), e2019EA000992. <https://doi.org/10.1029/2019ea000992>
- Määttänen, A., Montmessin, F., Gondet, B., Scholten, F., Hoffmann, H., González-Galindo, F., et al. (2010). Mapping the mesospheric CO₂ clouds on Mars: MEX/omega and MEX/HRSC observations and challenges for atmospheric models. *Icarus*, 209(2), 452–469. <https://doi.org/10.1016/j.icarus.2010.05.017>
- Määttänen, A., Pérot, K., Montmessin, F., & Hauchecorne, A. (2013). Mesospheric clouds on Mars and on Earth. *Comparative Climatology of Terrestrial Planets*, 393–413. https://doi.org/10.2458/azu_uapress_9780816530595-ch16
- Määttänen, A., Vehkamäki, H., Lauri, A., Merikallio, S., Kauhanen, J., Savijärvi, H., & Kulmala, M. (2005). Nucleation studies in the Martian atmosphere. *Journal of Geophysical Research*, 110(E2), E02002. <https://doi.org/10.1029/2004je002308>
- Madeleine, J.-B., Forget, F., Millour, E., Montabone, L., & Wolff, M. (2011). Revisiting the radiative impact of dust on Mars using the LMD global climate model. *Journal of Geophysical Research*, 116(E11), E11010. <https://doi.org/10.1029/2011je003855>
- Maltagliati, L., Montmessin, F., Fedorova, A., Korablev, O., Forget, F., & Bertaux, J.-L. (2011). Evidence of water vapor in excess of saturation in the atmosphere of Mars. *Science*, 333(6051), 1868–1871. <https://doi.org/10.1126/science.1207957>
- McCleese, D., Heavens, N., Schofield, J., Abdou, W., Bandfield, J., Calcutt, S., et al. (2010). Structure and dynamics of the Martian lower and middle atmosphere as observed by the Mars climate sounder: Seasonal variations in zonal mean temperature, dust, and water ice aerosols. *Journal of Geophysical Research*, 115(E12), E12016. <https://doi.org/10.1029/2010je003677>
- McConnochie, T., Bell, J., III, Savransky, D., Wolff, M., Toigo, A., Wang, H., et al. (2010). Themis-vis observations of clouds in the Martian mesosphere: Altitudes, wind speeds, and decimeter-scale morphology. *Icarus*, 210(2), 545–565. <https://doi.org/10.1016/j.icarus.2010.07.021>
- Mishchenko, M. I. (1991). Light scattering by randomly oriented axially symmetric particles. *Journal of the Optical Society of America A*, 8(6), 871–882. <https://doi.org/10.1364/josaa.8.000871>
- Mishchenko, M. I., & Travis, L. D. (1994). T-matrix computations of light scattering by large spheroidal particles. *Optics Communications*, 109(1–2), 16–21. [https://doi.org/10.1016/0030-4018\(94\)90731-5](https://doi.org/10.1016/0030-4018(94)90731-5)
- Montabone, L., Spiga, A., Kass, D. M., Kleinböhl, A., Forget, F., & Millour, E. (2020). Martian year 34 column dust climatology from Mars climate sounder observations: Reconstructed maps and model simulations. *Journal of Geophysical Research: Planets*, 125(8), e2019JE006111. <https://doi.org/10.1029/2019je006111>
- Montmessin, F., Forget, F., Rannou, P., Cabane, M., & Haberle, R. M. (2004). Origin and role of water ice clouds in the Martian water cycle as inferred from a general circulation model. *Journal of Geophysical Research*, 109(E10), E10004. <https://doi.org/10.1029/2004je002284>
- Montmessin, F., Quémerais, E., Bertaux, J.-L., Korablev, O., Rannou, P., & Lebonnois, S. (2006). Stellar occultations at UV wavelengths by the SPICAM instrument: Retrieval and analysis of Martian haze profiles. *Journal of Geophysical Research*, 111(E9), E09S09. <https://doi.org/10.1029/2005je002662>
- Montmessin, F., Rannou, P., & Cabane, M. (2002). New insights into Martian dust distribution and water-ice cloud microphysics. *Journal of Geophysical Research*, 107(E6), 4-1–4-14. <https://doi.org/10.1029/2001JE001520>
- Munguira, A., Hueso, R., Sánchez-Lavega, A., Torre-Juarez, M. D. L., Martínez, G., Newman, C., et al. (2022). Near surface atmospheric temperatures at Jezero from Mars 2020 MEDA measurements. *Journal of Geophysical Research: Planets*, 128, e2022JE007559. <https://doi.org/10.1029/2022JE007559>
- Navarro, T., Madeleine, J.-B., Forget, F., Spiga, A., Millour, E., Montmessin, F., & Määttänen, A. (2014). Global climate modeling of the Martian water cycle with improved microphysics and radiatively active water ice clouds. *Journal of Geophysical Research: Planets*, 119(7), 1479–1495. <https://doi.org/10.1002/2013je004550>
- Pollack, J. B., & Cuzzi, J. N. (1980). Scattering by nonspherical particles of size comparable to a wavelength: A new semi-empirical theory and its application to tropospheric aerosols. *Journal of the Atmospheric Sciences*, 37(4), 868–881. [https://doi.org/10.1175/1520-0469\(1980\)037<0868:sbnpos>2.0.co;2](https://doi.org/10.1175/1520-0469(1980)037<0868:sbnpos>2.0.co;2)
- Rannou, P., Perrier, S., Bertaux, J.-L., Montmessin, F., Korablev, O., & Reberac, A. (2006). Dust and cloud detection at the Mars limb with UV scattered sunlight with SPICAM. *Journal of Geophysical Research*, 111(E9), E09S10. <https://doi.org/10.1029/2006je002693>
- Rannou, P., Toledo, D., Lavvas, P., D'aversa, E., Moriconi, M., Adriani, A., et al. (2016). Titan's surface spectra at the Huygens landing site and Shangri-la. *Icarus*, 270, 291–306. <https://doi.org/10.1016/j.icarus.2015.09.016>
- Rodríguez-Manfredi, J. A., & de la Torre Juárez, M. (2021). Mars 2020 perseverance rover Mars environmental dynamics analyzer (MEDA) experiment data record (EDR) and reduced data record (RDR) data products archive bundle [Dataset]. PDS Atmospheres Node. Retrieved from https://arcnav.psi.edu/urn:nasa:pds:mars2020_meda/browse_skycam
- Rodríguez-Manfredi, J. A., De la Torre Juárez, M., Alonso, A., Apéstigue, V., Arruego, I., Atienza, T., et al. (2021). The Mars environmental dynamics analyzer, MEDA. A suite of environmental sensors for the Mars 2020 mission. *Space Science Reviews*, 217(3), 1–86. <https://doi.org/10.1007/s11214-021-00816-9>
- Rodríguez-Manfredi, J. A., de la Torre Juárez, M., Sánchez-Lavega, A., Hueso, R., Martínez, G., Lemmon, M., et al. (2023). The diverse meteorology of jezero crater over the first 250 sols of perseverance on Mars. *Nature Geoscience*, 16, 1–10. <https://doi.org/10.1038/s41561-022-01084-0>
- Sánchez-Lavega, A., Chen-Chen, H., Ordóñez-Etxeberria, I., Hueso, R., del Río-Gaztelurrutia, T., Garro, A., et al. (2018). Limb clouds and dust on Mars from images obtained by the visual monitoring camera (VMC) onboard Mars express. *Icarus*, 299, 194–205. <https://doi.org/10.1016/j.icarus.2017.07.026>
- Sánchez-Lavega, A., Río-Gaztelurrutia, T. D., Hueso, R., Juárez, M. D. L. T., Martínez, G., Harri, A.-M., et al. (2022). Mars 2020 perseverance rover studies of the Martian atmosphere over Jezero from pressure measurements. *Journal of Geophysical Research: Planets*, 128, e2022JE007480. <https://doi.org/10.1029/2022JE007480>

- Smith, M. D. (2009). Themis observations of Mars aerosol optical depth from 2002–2008. *Icarus*, 202(2), 444–452. <https://doi.org/10.1016/j.icarus.2009.03.027>
- Smith, M. D., Badri, K., Atwood, S. A., Edwards, C. S., Christensen, P. R., Wolff, M. J., et al. (2022). EMIRS observations of the aphelion-season Mars atmosphere. *Geophysical Research Letters*, 49(15), e2022GL099636. <https://doi.org/10.1029/2022gl099636>
- Smith, M. D., Martínez, G. M., Sebastián, E., Lemmon, M. T., Wolff, M. J., Apéstigue, V., et al. (2023). Diurnal and seasonal variations of aerosol optical depth observed by MEDA/TIRS at Jezero Crater, Mars. *Journal of Geophysical Research: Planets*, 128(1), e2022JE007560. <https://doi.org/10.1029/2022je007560>
- Smith, M. D., Wolff, M. J., Clancy, R. T., Kleinböhl, A., & Murchie, S. L. (2013). Vertical distribution of dust and water ice aerosols from CRISM limb-geometry observations. *Journal of Geophysical Research: Planets*, 118(2), 321–334. <https://doi.org/10.1002/jgre.20047>
- Smith, P. H., & Lemmon, M. (1999). Opacity of the Martian atmosphere measured by the imager for Mars pathfinder. *Journal of Geophysical Research*, 104(E4), 8975–8985. <https://doi.org/10.1029/1998je900017>
- Stcherbinine, A., Montmessin, F., Vincendon, M., Wolff, M. J., Vals, M., Korablev, O., et al. (2022). A two Martian years survey of water ice clouds on Mars with ACS onboard TGO. *Journal of Geophysical Research: Planets*, 127(12), e2022JE007502. <https://doi.org/10.1029/2022je007502>
- Tamppari, L. K., Zurek, R., & Paige, D. (2003). Viking-era diurnal water-ice clouds. *Journal of Geophysical Research*, 108(E7), 5073. <https://doi.org/10.1029/2002je001911>
- Toledo, D. (2023). Twilight mesospheric clouds in Jezero as observed by MEDA radiation and dust sensor (RDS) [Dataset]. Zenodo. <https://doi.org/10.5281/zenodo.7932426>
- Toledo, D., Arruero, I., Apéstigue, V., Jiménez, J., Gómez, L., Yela, M., et al. (2017). Measurement of dust optical depth using the solar irradiance sensor (SIS) onboard the exomars 2016 EDM. *Planetary and Space Science*, 138, 33–43. <https://doi.org/10.1016/j.pss.2017.01.015>
- Toledo, D., Rannou, P., Pommereau, J.-P., & Foujols, T. (2016). The optical depth sensor (ODS) for column dust opacity measurements and cloud detection on Martian atmosphere. *Experimental Astronomy*, 42(1), 61–83. <https://doi.org/10.1007/s10686-016-9500-7>
- Toledo, D., Rannou, P., Pommereau, J.-P., Sarkissian, A., & Foujols, T. (2016). Measurement of aerosol optical depth and sub-visual cloud detection using the optical depth sensor (ODS). *Atmospheric Measurement Techniques*, 9(2), 455–467. <https://doi.org/10.5194/amt-9-455-2016>
- Wang, H., & Ingersoll, A. P. (2002). Martian clouds observed by Mars global surveyor Mars orbiter camera. *Journal of Geophysical Research*, 107(E10), 8-1–8-16. <https://doi.org/10.1029/2001JE001815>
- Warren, S. G. (1984). Optical constants of ice from the ultraviolet to the microwave. *Applied Optics*, 23(8), 1206–1225. <https://doi.org/10.1364/ao.23.001206>
- West, R., Del Genio, A., Barbara, J., Toledo, D., Lavvas, P., Rannou, P., et al. (2016). Cassini imaging science subsystem observations of Titan's south polar cloud. *Icarus*, 270, 399–408. <https://doi.org/10.1016/j.icarus.2014.11.038>
- Wolff, M. J., Clancy, R. T., Goguen, J. D., Malin, M. C., & Cantor, B. A. (2010). Ultraviolet dust aerosol properties as observed by MARCI. *Icarus*, 208(1), 143–155. <https://doi.org/10.1016/j.icarus.2010.01.010>
- Wolff, M. J., Clancy, R. T., Kahre, M. A., Haberle, R. M., Forget, F., Cantor, B. A., & Malin, M. C. (2019). Mapping water ice clouds on Mars with MRO/MARCI. *Icarus*, 332, 24–49. <https://doi.org/10.1016/j.icarus.2019.05.041>
- Wolff, M. J., Fernando, A., Smith, M. D., Forget, F., Millour, E., Atwood, S. A., et al. (2022). Diurnal variations in the aphelion cloud belt as observed by the emirates exploration imager (EXI). *Geophysical Research Letters*, 49(18), e2022GL100477. <https://doi.org/10.1029/2022gl100477>
- Wolff, M. J., Smith, M., Clancy, R., Arvidson, R., Kahre, M., Seelos Iv, F., et al. (2009). Wavelength dependence of dust aerosol single scattering albedo as observed by the compact reconnaissance imaging spectrometer. *Journal of Geophysical Research*, 114(E2), E00D04. <https://doi.org/10.1029/2009je003350>